INTERNATIONAL JOURNAL FOR NUMERICAL METHODS IN ENGINEERING
Int. J. Numer. Meth. Engng 2011; **85**:1633–1647
Published online 28 September 2010 in Wiley Online Library (wileyonlinelibrary.com). DOI: 10.1002/nme.3034

On the long time simulation of the Rayleigh–Taylor instability

Hyun Geun Lee[1], Kyoungmin Kim[2] and Junseok Kim[1,*,†]

[1]*Department of Mathematics, Korea University, Seoul 136-701, Republic of Korea*
[2]*Department of Computer Science, Korea University, Seoul 136-701, Republic of Korea*

SUMMARY

We investigate the classical Rayleigh–Taylor instability with a phase-field method. Despite of the long history of numerical simulations for the Rayleigh–Taylor instability, almost all results were relatively short time experiments. This is partly because of the way of treating the pressure boundary conditions. We implement a time-dependent pressure boundary condition through a time-dependent density field at the boundary. Owing to the pressure boundary treatment, we can perform long time evolutions resulting in an equilibrium state. In addition to the bubble and spike fronts, we have found that the width of sides is another important landmark on the interface of the Rayleigh–Taylor instability. Copyright © 2010 John Wiley & Sons, Ltd.

Received 15 March 2010; Revised 27 July 2010; Accepted 28 July 2010

KEY WORDS: Rayleigh–Taylor instability; phase-field; multiphase flow; projection method

1. INTRODUCTION

When a heavy fluid is superposed over a light fluid in a gravitational field, the fluid interface is unstable. Any perturbation of this interface tends to grow with time, producing the phenomena known as the Rayleigh–Taylor instability. The phenomena are the penetration of both heavy and light fluids into each other. The Rayleigh–Taylor instability for a fluid in a gravitational field was originally introduced by Rayleigh [1] and later applied to all accelerated fluids by Taylor [2]. This instability has been applied to a wide range of problems, such as inertial confinement fusion [3], supernova explosion [4], nuclear weapon explosion [5], oceanography [6], atmospheric physics [7], and supernova remnant [8].

Many numerical methods have been proposed to study the Rayleigh–Taylor instability, including boundary integral methods [9–12], front tracking methods [13–15], volume of fluid methods [16, 17], lattice Boltzmann methods [18–20], level set methods [21–23], and phase-field methods [24–26]. Although there are many numerical studies [2, 9, 10, 12, 18, 23, 24, 26–28] with short time or large time simulation of the Rayleigh–Taylor instability, much less has been conducted long time simulation of the instability. To the authors' best knowledge, in the numerous papers found in the literature, the calculations were stopped well before the system reached the equilibrium configuration. Long time simulation of the Rayleigh–Taylor instability can be applied to a gravity separator for separating oil and water. Complete separation time is the one of important factors in designing the separator. With the previous methods, we do not evaluate a sufficient time to allow the oil and water phases to separate by gravity. But, by a numerical simulation, we can calculate a fully separation time of the mixture and use that time in deciding the length of the gravity

*Correspondence to: Junseok Kim, Department of Mathematics, Korea University, Seoul 136-701, Republic of Korea.
†E-mail: cfdkim@korea.ac.kr

separator. Therefore, an efficient and accurate numerical solution of long time evolution is needed to better understand the Rayleigh–Taylor instability.

The governing equations for time-dependent incompressible viscous fluids are the Navier–Stokes equations, together with the continuity and phase-field equations which are dimensional form become

$$\rho(\phi)(\mathbf{u}_t+\mathbf{u}\cdot\nabla\mathbf{u})=-\nabla p+\eta\Delta\mathbf{u}+\rho(\phi)\mathbf{g}, \tag{1}$$

$$\nabla\cdot\mathbf{u}=0, \tag{2}$$

$$\phi_t+\nabla\cdot(\phi\mathbf{u})=M\Delta\mu, \tag{3}$$

$$\mu=\alpha\phi^3-\beta\phi-k\Delta\phi, \tag{4}$$

where $\mathbf{u}$ is the velocity, p is the pressure, $\rho(\phi)=\rho_1(1-\phi)/2+\rho_2(1+\phi)/2$ is the density, η is the viscosity, $\mathbf{g}=(0,-g)$ is the gravity, M is the mobility, μ is the generalized chemical potential. In this paper the effect of the surface tension is negligible. We note that even though our phase-field model can deal with a variable viscosity case straightforwardly, we focus on the viscosity matched case since we are interested in long time simulation.

The paper is organized as follows. In Section 2, we derive the discrete scheme and numerical solution. We also present the approximate projection method used to solve the discrete Navier–Stokes equations. The numerical results are presented in Section 3. In Section 4, conclusions are drawn.

2. NUMERICAL SOLUTION

An efficient approximation can be obtained by decoupling the solution of the momentum equations from the solution of the continuity equation by a projection method [29–34]. The extension to 3D is straightforward. We will focus on describing the idea in two-dimensions.

A staggered marker-and-cell mesh of Harlow and Welch [35] is used in which pressure and phase fields are stored at cell centers and velocities at cell interfaces (Figure 1).

Let a computational domain be partitioned in Cartesian geometry into a uniform mesh with mesh spacing h. The center of each cell, Ω_{ij}, is located at $(x_i, y_j)=((i-0.5)h,(j-0.5)h)$ for $i=1,\ldots,N_x$ and $j=1,\ldots,N_y$. N_x and N_y are the numbers of cells in the x- and y-directions, respectively. The cell vertices are located at $(x_{i+1/2}, y_{j+1/2})=(ih, jh)$. We denote by ∇_d, $\nabla_d\cdot$,

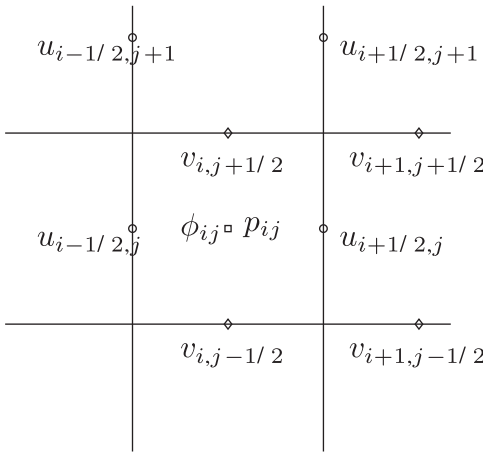

Figure 1. Velocities are defined at cell boundaries while the pressure and phase field are defined at the cell centers.

DOI: 10.1002/nme

and Δ_d the discrete gradient, divergence, and Laplacian, respectively. These are described in Equations (7) and (11).

At the beginning of each time step, given $\mathbf{u}^n$, ϕ^n, and p^n, we want to find $\mathbf{u}^{n+1}$, ϕ^{n+1}, and p^{n+1} which solve the following temporal discretization of dimensionless form of Equations (1)–(4) of motion:

$$\rho^n \frac{\mathbf{u}^{n+1}-\mathbf{u}^n}{\Delta t} = -\rho^n(\mathbf{u}\cdot\nabla_d\mathbf{u})^n - \nabla_d p^{n+1} + \frac{1}{Re}\Delta_d\mathbf{u}^n + \frac{\rho^n}{Fr}\mathbf{g},$$

$$\nabla_d\cdot\mathbf{u}^{n+1} = 0,$$

$$\frac{\phi^{n+1}-\phi^n}{\Delta t} = \frac{1}{Pe}\Delta_d v^{n+1} - \frac{1}{Pe}\Delta_d\phi^n - \nabla_d\cdot(\phi\mathbf{u})^n, \tag{5}$$

$$v^{n+1} = (\phi^{n+1})^3 - \varepsilon^2\Delta_d\phi^{n+1}, \tag{6}$$

where $\rho^n=\rho(\phi^n)$ and $\mathbf{g}=(0,-1)$. The dimensionless parameters are the Reynolds number, $Re=\rho_c U_c L_c/\eta$, the Froude number, $Fr=U_c^2/(gL_c)$, the Peclet number, $Pe=U_c L_c/(M\mu_c)$, and the Cahn number, $\varepsilon=\sqrt{k/(\alpha L_c^2)}$. The derivation of dimensionless form of Equations (1)–(4) is given in the Appendix.

The outline of the main procedures in one time step is:

Step 1. Initialize $\mathbf{u}^0$ to be the divergence-free velocity field and ϕ^0.

Step 2. Solve an intermediate velocity field, $\tilde{\mathbf{u}}$, which generally does not satisfy the incompressible condition, without the pressure gradient term,

$$\frac{\tilde{\mathbf{u}}-\mathbf{u}^n}{\Delta t} = -\mathbf{u}^n\cdot\nabla_d\mathbf{u}^n + \frac{1}{\rho^n Re}\Delta_d\mathbf{u}^n + \frac{1}{Fr}\mathbf{g}.$$

The resulting finite difference equations are written out explicitly. They take the form

$$\begin{aligned}
\tilde{u}_{i+1/2,j} &= u^n_{i+1/2,j} - \Delta t(uu_x+vu_y)^n_{i+1/2,j} \\
&\quad + \frac{\Delta t}{h^2\rho^n_{i+1/2,j}Re}(u^n_{i+3/2,j}+u^n_{i-1/2,j}-4u^n_{i+1/2,j}+u^n_{i+1/2,j+1}+u^n_{i+1/2,j-1}), \\
\tilde{v}_{i,j+1/2} &= v^n_{i,j+1/2} - \Delta t(uv_x+vv_y)^n_{i,j+1/2} - \frac{\Delta t}{Fr} \\
&\quad + \frac{\Delta t}{h^2\rho^n_{i,j+1/2}Re}(v^n_{i+1,j+1/2}+v^n_{i-1,j+1/2}-4v^n_{i,j+1/2}+v^n_{i,j+3/2}+v^n_{i,j-1/2}),
\end{aligned} \tag{7}$$

where the advection terms, $(uu_x+vu_y)^n_{i+1/2,j}$ and $(uv_x+vv_y)^n_{i,j+1/2}$, are defined by:

$$(uu_x+vu_y)^n_{i+1/2,j} = u^n_{i+1/2,j}\bar{u}^n_{x_{i+1/2,j}} + \frac{v^n_{i,j-1/2}+v^n_{i+1,j-1/2}+v^n_{i,j+1/2}+v^n_{i+1,j+1/2}}{4}\bar{u}^n_{y_{i+1/2,j}},$$

$$(uv_x+vv_y)^n_{i,j+1/2} = \frac{u^n_{i-1/2,j}+u^n_{i-1/2,j+1}+u^n_{i+1/2,j}+u^n_{i+1/2,j+1}}{4}\bar{v}^n_{x_{i,j+1/2}} + v^n_{i,j+1/2}\bar{v}^n_{y_{i,j+1/2}}.$$

The values $\bar{u}^n_{x_{i+1/2,j}}$ and $\bar{u}^n_{y_{i+1/2,j}}$ are computed using the upwind procedure. The procedure is

$$\bar{u}^n_{x_{i+1/2,j}} = \begin{cases} \dfrac{u^n_{i+1/2,j}-u^n_{i-1/2,j}}{h} & \text{if } u^n_{i+1/2,j}>0 \\ \dfrac{u^n_{i+3/2,j}-u^n_{i+1/2,j}}{h} & \text{otherwise} \end{cases}$$

DOI: 10.1002/nme

and

$$\bar{u}^n_{y_{i+1/2,j}} = \begin{cases} \dfrac{u^n_{i+1/2,j} - u^n_{i+1/2,j-1}}{h} & \text{if } v^n_{i,j-1/2} + v^n_{i+1,j-1/2} + v^n_{i,j+1/2} + v^n_{i+1,j+1/2} > 0 \\ \dfrac{u^n_{i+1/2,j+1} - u^n_{i+1/2,j}}{h} & \text{otherwise.} \end{cases}$$

The quantities $\bar{v}^n_{x_{i,j+1/2}}$ and $\bar{v}^n_{y_{i,j+1/2}}$ are computed in a similar manner.

Then, we solve the following equations for the advanced pressure field at $(n+1)$ time step.

$$\frac{\mathbf{u}^{n+1} - \tilde{\mathbf{u}}}{\Delta t} = -\frac{1}{\rho^n} \nabla_d p^{n+1}, \tag{8}$$

$$\nabla_d \cdot \mathbf{u}^{n+1} = 0. \tag{9}$$

With application of the divergence operator to Equation (8), we find that the Poisson equation for the pressure at the advanced time $(n+1)$

$$\nabla_d \cdot \left(\frac{1}{\rho^n} \nabla_d p^{n+1} \right) = \frac{1}{\Delta t} \nabla_d \cdot \tilde{\mathbf{u}}, \tag{10}$$

where we have made use of Equation (9) and the terms are defined as follows:

$$\begin{aligned} \nabla_d \cdot \left(\frac{1}{\rho^n} \nabla_d p^{n+1}_{ij} \right) &= \frac{\dfrac{1}{\rho^n_{i+1/2,j}} p^{n+1}_{i+1,j} + \dfrac{1}{\rho^n_{i-1/2,j}} p^{n+1}_{i-1,j} + \dfrac{1}{\rho^n_{i,j+1/2}} p^{n+1}_{i,j+1} + \dfrac{1}{\rho^n_{i,j-1/2}} p^{n+1}_{i,j-1}}{h^2} \\ &\quad - \frac{\dfrac{1}{\rho^n_{i+1/2,j}} + \dfrac{1}{\rho^n_{i-1/2,j}} + \dfrac{1}{\rho^n_{i,j+1/2}} + \dfrac{1}{\rho^n_{i,j-1/2}}}{h^2} p^{n+1}_{ij}, \\ \nabla_d \cdot \tilde{\mathbf{u}}_{ij} &= \frac{\tilde{u}_{i+1/2,j} - \tilde{u}_{i-1/2,j}}{h} + \frac{\tilde{v}_{i,j+1/2} - \tilde{v}_{i,j-1/2}}{h}, \end{aligned} \tag{11}$$

where $\rho^n_{i+1/2,j} = (\rho^n_{ij} + \rho^n_{i+1,j})/2$ and the other terms are similarly defined.

The boundary condition for the pressure is

$$\mathbf{n} \cdot \nabla_d p^{n+1} = \mathbf{n} \cdot \left(-\rho^n \frac{\mathbf{u}^{n+1} - \mathbf{u}^n}{\Delta t} - \rho^n (\mathbf{u} \cdot \nabla_d \mathbf{u})^n + \frac{1}{Re} \Delta_d \mathbf{u}^n + \frac{\rho^n}{Fr} \mathbf{g} \right),$$

where $\mathbf{n}$ is the unit normal vector to the domain boundary.

In our application of the phase-field to the Rayleigh–Taylor instability, we will use a periodic boundary condition to vertical boundaries and no slip boundary condition to the top and bottom domain. Therefore,

$$\mathbf{n} \cdot \nabla_d p^{n+1} = \mathbf{n} \cdot \frac{\rho^n}{Fr} \mathbf{g} \quad \text{i.e. } \frac{\partial p}{\partial y} = -\frac{\rho^n}{Fr} \quad \text{at } y = 0 \quad \text{and} \quad y = L_y.$$

The resulting linear system of Equation (10) is solved using a multigrid method [36], specifically, V-cycles with a Gauss–Seidel relaxation. Then the divergence-free normal velocities u^{n+1} and v^{n+1} are defined by:

$$\mathbf{u}^{n+1} = \tilde{\mathbf{u}} - \frac{\Delta t}{\rho^n} \nabla_d p^{n+1} \quad \text{i.e.,}$$

$$u^{n+1}_{i+1/2,j} = \tilde{u}_{i+1/2,j} - \frac{\Delta t}{\rho^n_{i+1/2,j} h} (p_{i+1,j} - p_{ij}), \quad v^{n+1}_{i,j+1/2} = \tilde{v}_{i,j+1/2} - \frac{\Delta t}{\rho^n_{i,j+1/2} h} (p_{i,j+1} - p_{ij}).$$

DOI: 10.1002/nme

We implement the unconditionally gradient stable scheme in Equations (5) and (6) with a nonlinear multigrid method. For a detailed description of the numerical method used in solving these equations, please refer to References [37, 38].

Since we are interested in long time simulations, mass conservation is an important factor. Therefore, we use a conservative discretization of the convective part of the phase-field equation (5):

$$((\phi u)_x+(\phi v)_y)_{ij}^n=\frac{u_{i+1/2,j}^n(\phi_{i+1,j}^n+\phi_{ij}^n)-u_{i-1/2,j}^n(\phi_{ij}^n+\phi_{i-1,j}^n)}{2h}+\frac{v_{i,j+1/2}^n(\phi_{i,j+1}^n+\phi_{ij}^n)-u_{i,j-1/2}^n(\phi_{ij}^n+\phi_{i,j-1}^n)}{2h}.$$

These complete the one time step.

3. NUMERICAL RESULTS

In this section, we test the pressure boundary condition to validate the performance of the phase-field scheme. We also perform the following numerical tests for the Rayleigh–Taylor instability: effect of the Peclet number, convergence test, long time evolution, relation between the density ratio and interface length, relation between the Atwood number and the width of the bubble and spike fluid, evolution of interface with alternate density ratios, evolution of interface of random amplitude, and effect of the Capillary number. Note that, in these simulations, we used Equation (2) as the continuity equation since we focus on the pressure boundary treatment. However, in the case of the large density ratio, the continuity equation can no longer be reduced to Equation (2). In that case, we should use $\rho_t+\nabla\cdot(\rho\mathbf{u})=0$ as the continuity equation and we expect that the results would be different.

3.1. Pressure field distribution with different density ratios

The difference between the current scheme and previous studies of the Rayleigh–Taylor instability is the pressure boundary treatment. To demonstrate the ability of the current scheme, we test the pressure boundary condition for three cases with $\rho_1/\rho_2=1$, $\frac{1}{2}$, and $\frac{1}{4}$, respectively. In Figure 2, the circles represent the pressure with $\rho_1/\rho_2=1$, the stars that with $\rho_1/\rho_2=\frac{1}{2}$, the diamonds that with

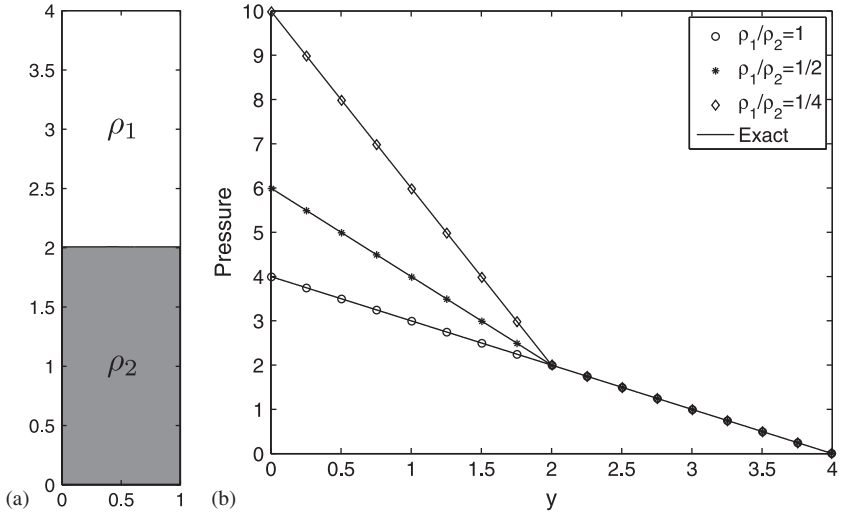

Figure 2. The pressure for different density ratios: the circles represent the pressure with $\rho_1/\rho_2=1$, the stars that with $\rho_1/\rho_2=\frac{1}{2}$, the diamonds that with $\rho_1/\rho_2=\frac{1}{4}$, and the solid line denotes the analytic solution.

DOI: 10.1002/nme

$\rho_1/\rho_2 = \frac{1}{4}$, and the solid line denotes the analytic solution. The pressure is decreasing and is in inverse proportion to density ratio. These numerical results agree well with the analytic solution.

3.2. Effect of the Peclet number

The Rayleigh–Taylor instability would occur for any perturbation along the interface between a heavy fluid on top of a lighter fluid and is characterized by the density ratio between the two fluids. The density difference is represented by the Atwood number $At = (\rho_2 - \rho_1)/(\rho_2 + \rho_1)$, where ρ_1 and ρ_2 are the densities of the lighter and heavier fluid, respectively. In this section, we investigate the effect of the Peclet number, demonstrate the convergence of our scheme numerically, and simulate the Rayleigh–Taylor instability for a long time. Unless otherwise specified, we take the initial state as

$$\phi(x, y, 0) = \tanh\left(\frac{y - 2 - 0.1\cos(2\pi x)}{\sqrt{2}\varepsilon}\right) \tag{12}$$

on the computational domain $\Omega = (0, 1) \times (0, 4)$, which represents a planar interface superimposed by a perturbation of wave number $k = 1$ and amplitude 0.1. The density ratio is $\rho_2 : \rho_1 = 3 : 1$, i.e. $At = 0.5$. We use the simulation parameters such as the uniform time step, $\Delta t = 0.00125\sqrt{2}$, $\varepsilon = 0.01$, and $Re = 3000$.

In order to investigate the effect of the Peclet number, we consider the evolution of the interface with different Peclet numbers. The initial state is given in Equation (12) and the zero-level set is shown in Figure 3(a). In this test, the number of grid points is 128×512. The evolutions of the interface with different Peclet numbers $Pe = 0.01/\varepsilon$, $1/\varepsilon$, and $100/\varepsilon$, respectively, are shown in Figures 3(b)–(d). In the case of $Pe = 0.01/\varepsilon$, the evolution of the interface did not fully happen (we cannot see the rolling-up of the falling fluid). And in the case of $Pe = 100/\varepsilon$, the contour line is not uniform. Therefore, the appropriate Peclet number is $Pe = 1/\varepsilon$. It is clear that the interface evolution is significantly affected by Pe numbers. Increasing Pe numbers results in non-smooth concentration profile, whereas decreasing Pe numbers results in too much diffusion. Unless otherwise mentioned, we use the Peclet number $Pe = 1/\varepsilon$ in our study.

3.3. Convergence test

We perform a number of simulations for a sample initial problem on a set of increasingly finer grids. The initial state is taken in Equation (12). The numerical solutions are computed on the

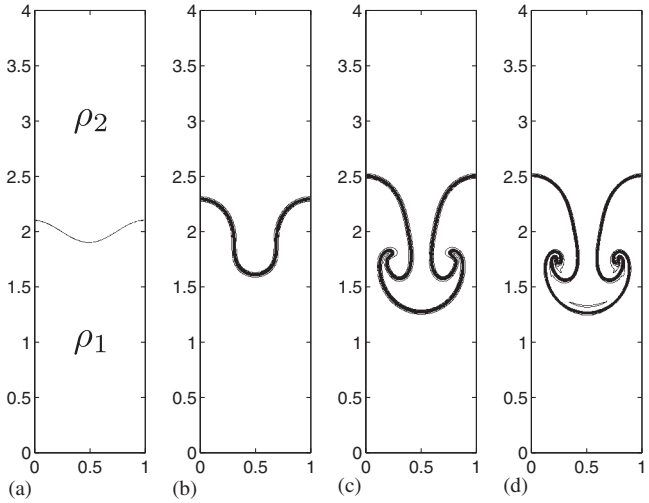

Figure 3. (a) The zero-level set of the initial profile, $\phi(x, y, 0) = \tanh((y - 2 - 0.1\cos(2\pi x))/\sqrt{2}\varepsilon)$. The effect of the Peclet number on the temporal evolution of the interface at dimensionless time $t = 1.75$: (b) $Pe = 0.01/\varepsilon$; (c) $Pe = 1/\varepsilon$; and (d) $Pe = 100/\varepsilon$. Contour levels are $-0.9, -0.7, \ldots, 0.7, 0.9$.

DOI: 10.1002/nme

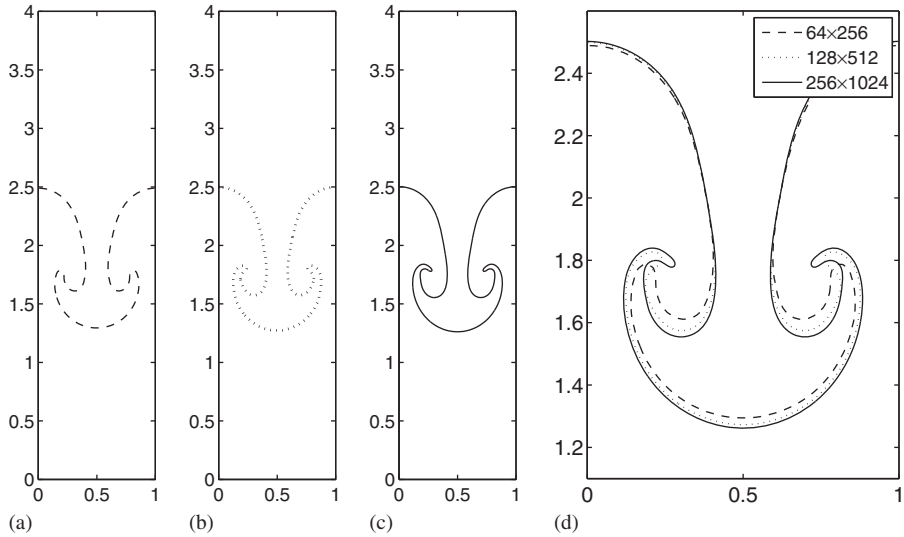

Figure 4. The evolution of the interface at dimensionless time $t=1.75$: (a) 64×256; (b) 128×512; and (c) 256×1024.

uniform grids, $h=1/2^n$, and with corresponding time steps, $\Delta t=0.16\sqrt{2}h$ for $n=6$, 7, and 8. For the interface parameter ε, we want to have smaller ε as the grid size h is refined. One possible choice is $\varepsilon=O(h^k)$, where k satisfy the condition, $0<k<1$. Note that k cannot be greater than one because we also want to have a finite number of grid points across interface. For the convergence test, we choose $k=\frac{1}{2}$, i.e. $\varepsilon=0.08\sqrt{2h}$. Other parameters are the same as used in Section 3.2. Figures 4(a)–(c) are the evolutions of the interface with different grid sizes 64×256, 128×512, and 256×1024, respectively. The main difference between Figures 4(a)–(c) is in the vortex. The vortices on the finest grid (256×1024) have a spiral, while on the coarsest grid (64×256)there is no rolling-up. The results suggest that the vortex depends on grid resolution (Figure 4(d)).

3.4. Long time evolution of the Rayleigh–Taylor instability

Figure 5 shows the y-coordinate of the top of the rising fluid (a bubble) and the bottom of the falling fluid (a spike). The initial state is given in Equation (12) (this is the same initial condition as H. Ding *et al.* [25], Guermond *et al.* [27], and Tryggvason [39]) and the number of grid points is 128×512. The results in Figure 5 show that our result and the previous results of H. Ding *et al.*, Guermond *et al.,* and Tryggvason are in good agreement. The evolution of the interface is shown in Figure 6 at $t=0$, 1, 1.5, 1.75, 2, 2.25, 2.5, 6, 8, 12, 18, 24, 30, and 50 in the time scale of Tryggvason which is related to ours by $t_{\text{Tryg}}=t\sqrt{At}$. The rolling-up of the falling fluid can be clearly seen. At time $t=50$, the heavier fluid has been fallen down completely.

3.5. Relation between the density ratio and the interface length

In this section, we consider the relation between the density ratio and the interface length. The interface length L is defined by

$$L(\phi)=\sum_{i=1}^{N_x}\sum_{j=1}^{N_y}\frac{3\sqrt{2}\varepsilon}{4}|\nabla_d\phi_{ij}|^2h^2,$$

where

$$\nabla_d\phi_{ij}=\left(\frac{\phi_{i+1,j}-\phi_{ij}}{h},\frac{\phi_{i,j+1}-\phi_{ij}}{h}\right)$$

DOI: 10.1002/nme

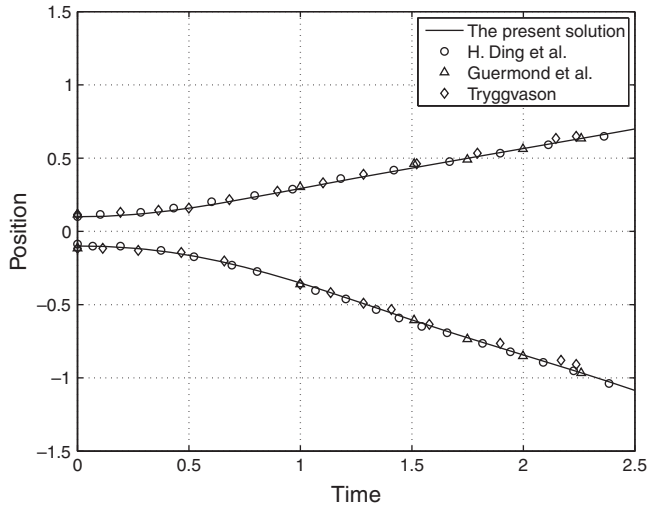

Figure 5. The y-coordinate of the tip of the falling and rising fluid versus dimensionless time: solid line denotes the present solution, the open circles represent the solution of H. Ding *et al.*, the open triangles that of Guermond *et al.*, and the open diamonds that of Tryggvason.

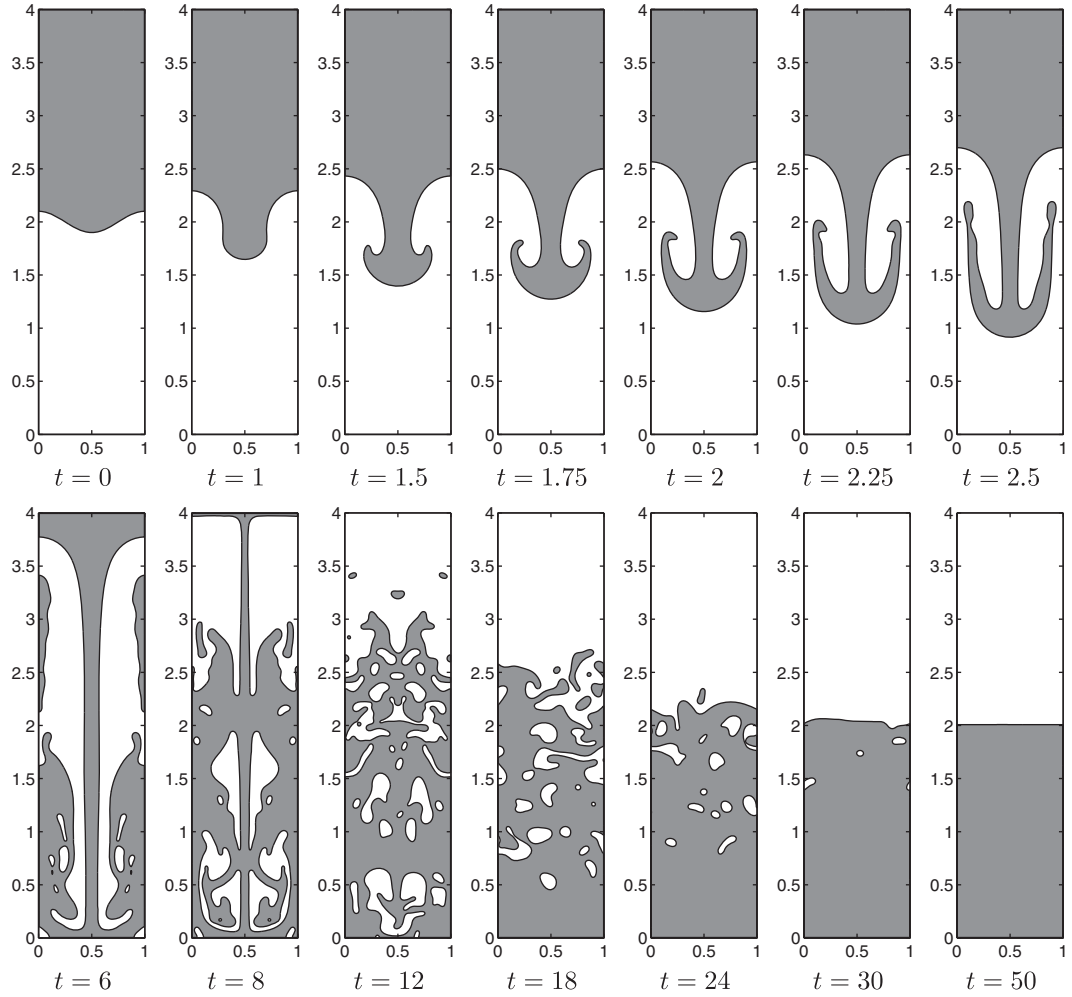

Figure 6. Long time evolution of the Rayleigh–Taylor instability simulation with $At = 0.5$. The dimensionless times are shown below each figure.

DOI: 10.1002/nme

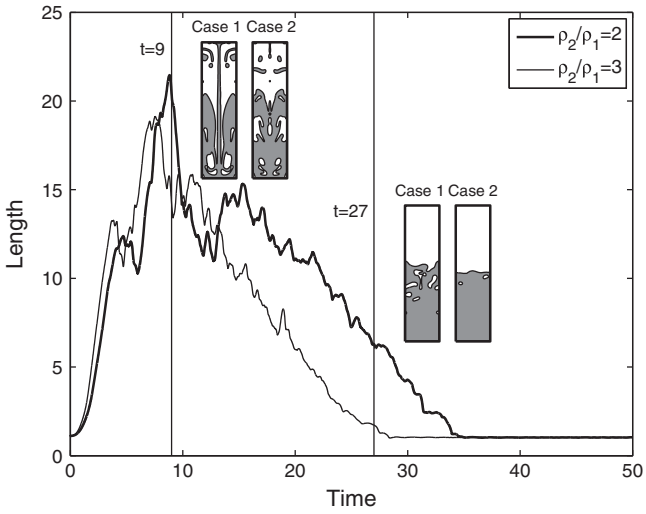

Figure 7. The interface length for different density ratios: the thick solid line represents the interface length with $\rho_2/\rho_1 = 2$ (Case 1) and the solid line that with $\rho_2/\rho_1 = 3$ (Case 2).

is a finite difference approximation to the gradient operator. The initial state is given in Equation (12) on $\Omega = (0,1)\times(0,4)$. We take $h = \frac{1}{64}$, $\varepsilon = 0.014$, and $Re = 3000$. The time steps corresponding to the density ratios, $\Delta t = 0.00125\sqrt{2}/(\rho_2/\rho_1)$, are used and the calculations are run up to dimensionless time $T = 50$. In Figure 7, the interface lengths (until the heavier fluid has been fallen down completely) with different density ratios are shown. The thick solid and solid line represents the interface length with $\rho_2/\rho_1 = 2$ and 3, respectively. The inscribed small figures are the concentration fields at the indicated dimensionless times. These results give us two conclusions. First, as the density ratio (ρ_2/ρ_1) is higher, the interface length approaches the equilibrium solution faster (the interface length, is equal to 1, represents that the numerical solution approaches the equilibrium solution). Second, as the density ratio is lower, the interface length grows longer. In case of high density ratio, an interface shape during evolution is simple. But in case of low density ratio, an interface shape during evolution is complex. Hence, many vortices, occur in low density ratio, make interface length long.

3.6. Relation between the Atwood number and the width of the bubble and spike fluid

Another important test is the comparison between the Atwood number and the width of the bubble and spike fluid. We simulate with a grid size 128×512 and a computational domain $\Omega = (0,1)\times(0,4)$. The initial condition is $\phi(x,y,0) = \tanh((y-2-0.05\cos(2\pi x))/\sqrt{2}\varepsilon)$ (Figure 8(a)), $\varepsilon = 0.01$, $\Delta t = 0.00125\sqrt{2}$, and $Re = 3000$ are used. The calculations are run up to the tip of the bubble until it reaches 2.5. The evolutions of the interface with different Atwood numbers $At = 0.1$, 0.2, 0.3, 0.4, and 0.5, respectively, are shown in Figures 8(b)–(f). We measure the width at the position of the half distance from two tangent lines (denoted by dashed lines) of bubble and spike (Figure 9(a)). Figure 9(b) shows the ratio of the width of the bubble (b_w) and spike (s_w) fluid versus the Atwood number. The ratio is in proportion to the Atwood number because the width of the bubble becomes wide and that of the spike becomes narrow.

3.7. Evolution of interface with alternate density ratios

In the simulations, a 128×512 mesh is used on $\Omega = (0,1)\times(0,4)$ and we employ $\Delta t = 0.00125\sqrt{2}$, $\varepsilon = 0.01$, $At = 0.5$, and $Re = 3000$. In the first experiment, we take the initial condition as shown in Figure 10(a) (first column). The wave number is $k = 1$ and amplitude is 0.1. The results are

DOI: 10.1002/nme

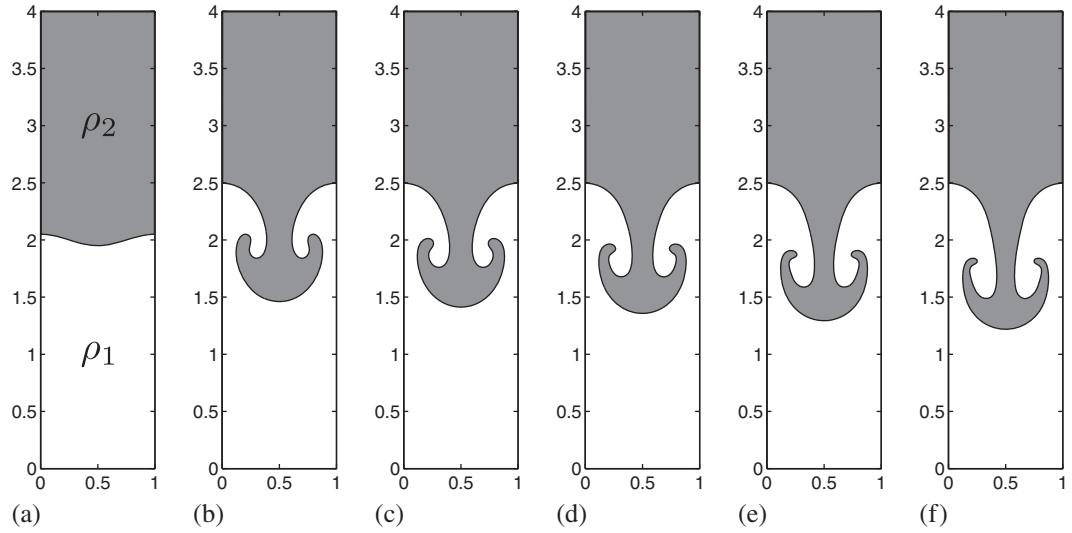

Figure 8. (a) The initial profile, $\phi(x, y, 0) = \tanh((y - 2 - 0.05\cos(2\pi x))/\sqrt{2}\varepsilon)$. (b), (c), (d), (e), and (f) are the evolutions of the interface with different Atwood numbers $At = 0.1$, 0.2, 0.3, 0.4, and 0.5, respectively.

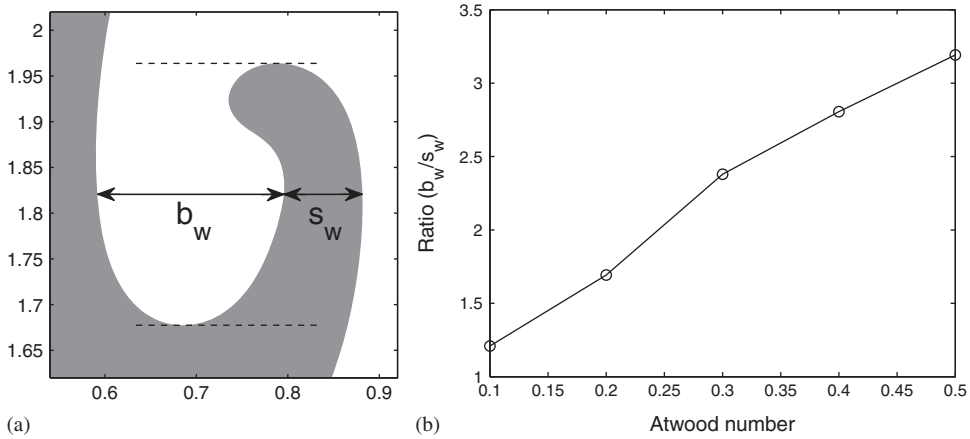

Figure 9. (a) We measure the width at the position of the half distance from two tangent lines (denoted by dashed lines) of bubble and spike and (b) The ratio of the width of the bubble (b_w) and spike (s_w) fluid versus Atwood number.

presented in Figure 10(a) (from second column to seventh column). In the second experiment, we take the initial condition as shown in Figure 10(b) (first column). The results are presented in Figure 10(b) (from second column to seventh column). Observe that the current scheme is robust.

3.8. Evolution of interface of random amplitude

In this section, we demonstrate the capability of the current scheme with complex initial configuration. The initial condition is $\phi(x, y, 0) = \tanh((y - 0.5 + 0.01\text{rand}(y))/\sqrt{2}\varepsilon)$, where the random number, rand(y), is in $[-1, 1]$ and has zero mean (Figure 11(a)). A 1024×256 mesh is used on $\Omega = (0, 4) \times (0, 1)$ and we choose $\Delta t = 0.00063\sqrt{2}$, $\varepsilon = 0.007$, $At = 0.5$, $Re = 3000$. The evolutions of the interface at dimensionless times $t = 1.5$, 2.0, and 2.5, respectively, are shown in Figures 11(b)–(d). As each row shows, the current scheme can straightforwardly deal with complex initial configuration.

DOI: 10.1002/nme

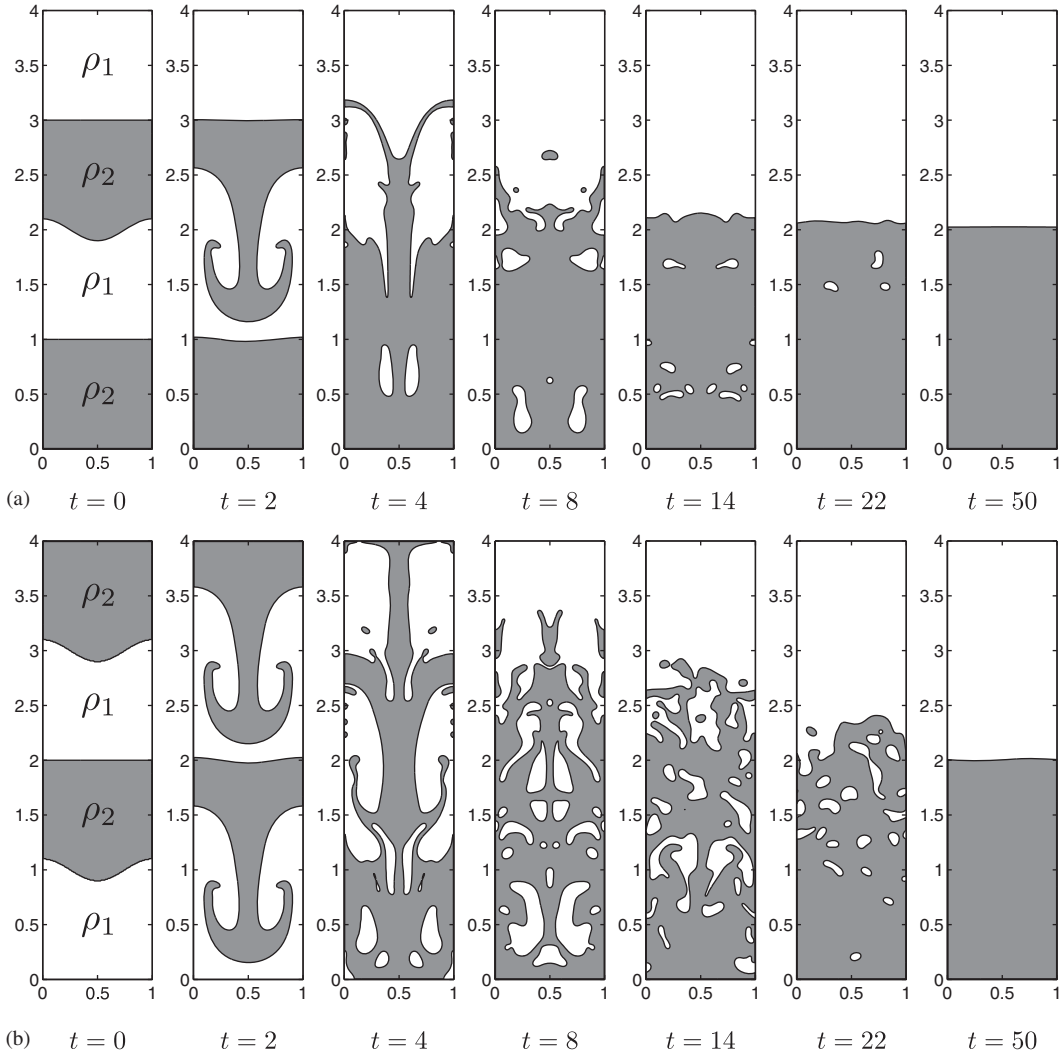

Figure 10. Long time evolution of the Rayleigh–Taylor instability simulation with $At = 0.5$. The dimensionless times are shown below each figure.

3.9. Effect of the capillary number

In order to investigate the effect of the Capillary number, we consider the following equations:

$$\rho(\phi)(\mathbf{u}_t + \mathbf{u}\cdot\nabla\mathbf{u}) = -\nabla p + \frac{1}{Re}\Delta\mathbf{u} - \frac{3\sqrt{2}\varepsilon}{4We}\nabla\cdot\left(\frac{\nabla\phi}{|\nabla\phi|}\right)|\nabla\phi|\nabla\phi + \frac{\rho(\phi)}{Fr}\mathbf{g},$$

$$\nabla\cdot\mathbf{u} = 0,$$

$$\phi_t + \nabla\cdot(\phi\mathbf{u}) = \frac{1}{Pe}\Delta\mu,$$

$$\mu = \phi^3 - \phi - \varepsilon^2\Delta\phi,$$

where the dimensionless parameter is the Weber number, $We = \rho_c U_c^2 L_c/\sigma$, and σ is the interfacial tension coefficient. The Capillary number represents the relative effect of viscous forces versus interfacial tension acting across an interface between two immiscible fluids. It is defined as $Ca = U_c\eta/\sigma$, i.e. $Ca = We/Re$.

DOI: 10.1002/nme

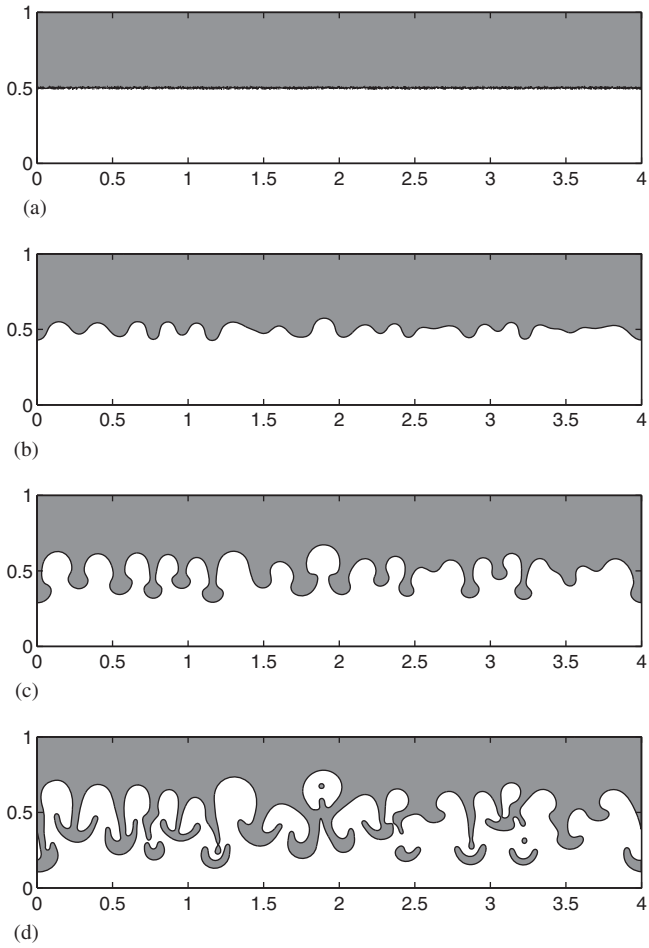

Figure 11. Evolution of interface of random amplitude. The dimensionless times are shown below each figure: (a) $t=0$; (b) $t=1.5$; (c) $t=2.0$; and (d) $t=2.5$.

To show how the Capillary number affects the stability, we take the initial state as given in Equation (12). A 128×512 mesh is used on $\Omega=(0,1)\times(0,4)$ and we employ $\Delta t=0.00125\sqrt{2}$, $\varepsilon=0.01$, $At=0.5$, and $Re=3000$. Figures 12(a) and (b) show evolutions of the interface with different Capillary number $Ca=0.1$ and 0.005, respectively. In the case of $Ca=0.1$, the Ca number is high (i.e. interfacial tension is low) compared with the gravitational force. As a result, the interface becomes unstable (Figure 12(a)). On the other hand, in the case of $Ca=0.005$, the interface becomes stable, though it started with the same initial perturbation. Because the Ca number is low compared with the gravitational force.

4. CONCLUSION

The purpose of this paper is twofold: to introduce a new computing method for the time-dependent calculation of the interaction of two incompressible fluids and to present new long time evolution results in the study of the Rayleigh–Taylor instability. The key to the success of the method is the treatment of the pressure boundary. To demonstrate the accuracy and efficiency of the method, we carried out numerical experiments such as pressure field distribution with different density ratios, effect of the Peclet number, convergence test, long time evolution, interface length with different density ratios, relation between Atwood number and width of the bubble and spike fluid, evolution

DOI: 10.1002/nme

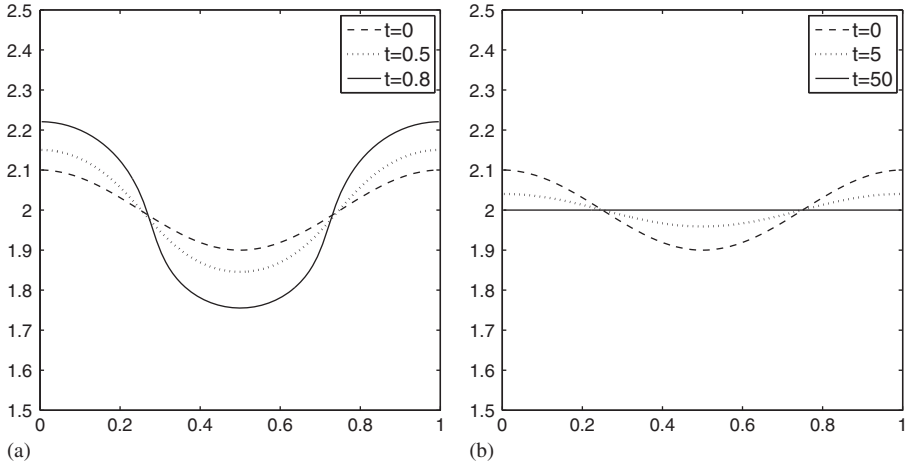

Figure 12. The effect of the Capillary number on the temporal evolution of the interface: (a) $Ca=0.1$ and (b) $Ca=0.005$.

of interface with alternate density ratios, evolution of interface of random amplitude, and effect of the Capillary number.

Our main concern in this paper was the pressure boundary condition for two incompressible fluids. Owing to the pressure boundary treatment, we could perform long time evolution of the Rayleigh–Taylor instability with small Atwood number. Usually, the density ratio cannot be very large because of the numerical instability. With the large density ratio, the continuity equation can no longer be reduced to $\nabla\cdot\mathbf{u}=0$. As a future research plan, the new pressure boundary condition will be applied to the compressible Navier–Stokes–Cahn–Hilliard equations (NSCH):

$$
\begin{aligned}
(\rho\mathbf{u})_t+\nabla\cdot(\rho\mathbf{u}\mathbf{u}) &= -\nabla p+\frac{1}{Re}\Delta\mathbf{u}+\frac{\rho}{Fr}\mathbf{g},\\
\rho_t+\nabla\cdot(\rho\mathbf{u}) &= 0,\\
\phi_t+\nabla\cdot(\phi\mathbf{u}) &= \frac{1}{Pe}\Delta\mu,\\
\mu &= \phi^3-\phi-\varepsilon^2\Delta\phi.
\end{aligned}
$$

APPENDIX A: NONDIMENSIONAL GOVERNING EQUATION

To restate the dimensional NSCH system in dimensionless form, we define the dimensionless variables as

$$
x'=\frac{x}{L_\mathrm{c}},\quad \mathbf{u}'=\frac{\mathbf{u}}{U_\mathrm{c}},\quad t'=\frac{tU_c}{L_\mathrm{c}},\quad p'=\frac{p}{\rho_\mathrm{c}U_\mathrm{c}^2},\quad \mathbf{g}'=\frac{\mathbf{g}}{g},\quad \rho'=\frac{\rho}{\rho_\mathrm{c}},\quad \mu'=\frac{\mu}{\mu_c},
$$

where L_c is the characteristic length, which is taken to be the shortest length of the problem domain in the axial direction, U_c is the characteristic velocity, ρ_c is the characteristic density defined as that of light fluid, i.e. $\rho_\mathrm{c}=\rho_1$, g is the gravitational acceleration, and μ_c is α, which is $\mu=\alpha(\phi^3-\frac{\beta}{\alpha}\phi-\frac{k}{\alpha}\Delta\phi)=\mu_c\mu'$. Substituting these variables into the governing Equations (1)–(4) we have

$$
\rho'(\mathbf{u}'_{t'}+\mathbf{u}'\cdot\nabla'\mathbf{u}')=-\nabla' p'+\frac{\eta}{\rho_\mathrm{c}U_\mathrm{c}L_\mathrm{c}}\Delta'\mathbf{u}'+\frac{gL_\mathrm{c}}{U_\mathrm{c}^2}\rho'\mathbf{g}', \tag{A1}
$$

$$
\nabla'\cdot\mathbf{u}'=0, \tag{A2}
$$

DOI: 10.1002/nme

$$\phi_{t'} + \nabla' \cdot (\phi \mathbf{u}') = \frac{M\mu_c}{U_c L_c} \Delta' \mu', \tag{A3}$$

$$\mu' = \phi^3 - \frac{\beta}{\alpha}\phi - \frac{k}{\alpha L_c^2}\Delta\phi. \tag{A4}$$

Dropping the primes and considering $\alpha = \beta$, Equations (A1)–(A4) become

$$\rho(\mathbf{u}_t + \mathbf{u} \cdot \nabla \mathbf{u}) = -\nabla p + \frac{1}{Re}\Delta \mathbf{u} + \frac{\rho}{Fr}\mathbf{g},$$

$$\nabla \cdot \mathbf{u} = 0,$$

$$\phi_t + \nabla \cdot (\phi \mathbf{u}) = \frac{1}{Pe}\Delta\mu,$$

$$\mu = \phi^3 - \phi - \varepsilon^2 \Delta\phi.$$

The dimensionless physical parameters are the Reynolds number, Re, Froude number, Fr, Peclet number, Pe, Cahn number, ε, given by

$$\mathrm{Re} = \frac{\rho_c U_c L_c}{\eta}, \quad Fr = \frac{U_c^2}{g L_c}, \quad Pe = \frac{U_c L_c}{M\mu_c}, \quad \varepsilon = \sqrt{\frac{k}{\alpha L_c^2}}.$$

Using $U_c = (gL_c)^{1/2}$, we have $Re = \rho_c U_c L_c/\eta = \rho_c g^{1/2} {L_c}^{3/2}/\eta$ and $Fr = U_c^2/gL_c = gL_c/gL_c = 1$.

ACKNOWLEDGEMENTS

This research was supported by Basic Science Research Program through the National Research Foundation of Korea (NRF) funded by the Ministry of Education, Science and Technology (NO. R01-2008-000-20855-0).

REFERENCES

1. Rayleigh L. Investigation of the character of the equilibrium of an incompressible heavy fluid of variable density. *Proceedings of the London Mathematical Society* 1883; **14**:170–177.
2. Taylor G. The instability of liquid surfaces when accelerated in a direction perpendicular to their planes. I. *Proceedings of the Royal Society of London, Series A* 1950; **201**:192–196.
3. Atzeni S, Meyer-Ter-Vehn J. *The Physics of Inertial Fusion: Beam Plasma Interaction, Hydrodynamics, Hot Dense Matter*. Oxford University Press: New York, 2004.
4. Buchler JR, Livio M, Colgate SA. Supernova explosions—the role of a Rayleigh–Taylor instability. *Space Science Review* 1980; **27**:571–577.
5. Brecht SH, Papadopoulos K. *Cross Field Jetting of Energetic Ions Produced by Rayleigh–Taylor Instability*. Naval Research Lab: Washington, 2002.
6. Debnath L. *Nonlinear Water Waves*. Academic Press: Boston, 1994.
7. Keskinen MJ, Ossakow SL, Szuszczewicz EP, Holmes JC. Nonlinear theory and experimental observations of the local collisional Rayleigh–Taylor instability in a descending equatorial spread F ionosphere. *Journal of Geophysical Research* 1981; **86**:5785–5792.
8. Ribeyre X, Tikhonchuk VT, Bouquet S. Compressible Rayleigh–Taylor instabilities in supernova remnants. *Physics of Fluids* 2004; **16**:4661–4670.
9. Baker GR, Meiron DI, Orszag SA. Vortex simulations of the Rayleigh–Taylor instability. *Physics of Fluids* 1980; **23**:1485–1490.
10. Baker GR, Meiron DI, Orszag SA. Boundary integral methods for axisymmetric and three-dimensional Rayleigh–Taylor instability problems. *Physica D* 1984; **12**:19–31.
11. Duchemin L, Josserand C, Clavin P. Asymptotic behavior of the Rayleigh–Taylor instability. *Physical Review Letters* 2005; **94**:224501-1–224501-4.
12. Verdon CP, McCrory RL, Morse RL, Baker GR, Meiron DI, Orszag SA. Nonlinear effects of multifrequency hydrodynamic instabilities on ablatively accelerated thin shells. *Physics of Fluids* 1982; **25**:1653–1674.
13. Popinet S, Zaleski S. A front-tracking algorithm for accurate representation of surface tension. *International Journal for Numerical Methods in Fluids* 1999; **30**:775–793.
14. Tryggvason G, Bunner B, Esmaeeli A, Juric D, Al-Rawahi N, Tauber W, Han J, Nas S, Jan Y-J. A front-tracking method for the computations of multiphase flow. *Journal of Computational Physics* 2001; **169**:708–759.

DOI: 10.1002/nme

15. Unverdi SO, Tryggvason G. A front-tracking method for viscous, incompressible, multi-fluid flows. *Journal of Computational Physics* 1992; **100**:25–37.
16. Gerlach D, Tomar G, Biswas G, Durst F. Comparison of volume-of-fluid methods for surface-tension dominant two-phase flows. *International Journal of Heat and Mass Transfer* 2006; **49**:740–754.
17. Hirt CW, Nichols BD. Volume of fluid (VOF) method for the dynamics of free boundaries. *Journal of Computational Physics* 1981; **39**:201–225.
18. He X, Chen S, Zhang R. A lattice Boltzmann scheme for incompressible multiphase flow and its application in simulation of Rayleigh–Taylor instability. *Journal of Computational Physics* 1999; **152**:642–663.
19. He X, Zhang R, Chen S, Doolen GD. On the three-dimensional Rayleigh–Taylor instability. *Physics of Fluids* 1999; **11**:1143–1152.
20. Nie X, Qian Y-H, Doolen GD, Chen S. Lattice Boltzmann simulation of the two-dimensional Rayleigh–Taylor instability. *Physical Review E* 1998; **58**:6861–6864.
21. Chang YC, Hou TY, Merriman B, Osher S. Eulerian capturing methods based on a level set formulation for incompressible fluid interfaces. *Journal of Computational Physics* 1996; **124**:449–464.
22. Gomez P, Hernandez J, Lopez J. On the reinitialization procedure in a narrow-band locally refined level set method for interfacial flows. *International Journal for Numerical Methods in Engineering* 2005; **63**:1478–1512.
23. Sussman M, Smereka P, Osher S. A level set approach for computing solutions to incompressible two-phase flow. *Journal of Computational Physics* 1994; **114**:146–159.
24. Celani A, Mazzino A, Muratore-Ginanneschi P, Vozella L. Phase-field model for the Rayleigh–Taylor instability of immiscible fluids. *The Journal of Fluid Mechanics* 2009; **622**:115–134.
25. Ding H, Spelt PDM, Shu C. Diffuse interface model for incompressible two-phase flows with large density ratios. *Journal of Computational Physics* 2007; **226**:2078–2095.
26. Jacqmin D. Calculation of two-phase Navier–Stokes flows using phase-field modeling. *Journal of Computational Physics* 1999; **155**:96–127.
27. Guermond J-L, Quartapelle L. A projection FEM for variable density incompressible flows. *Journal of Computational Physics* 2000; **165**:167–188.
28. Remacle J-F, Shephard MS. An algorithm oriented mesh database. *International Journal for Numerical Methods in Engineering* 2003; **58**:349–374.
29. Bell JB, Colella P, Glaz HM. A second-order projection method for the incompressible Navier–Stokes equations. *Journal of Computational Physics* 1989; **85**:257–283.
30. Chorin AJ. A numerical method for solving incompressible viscous flow problems. *Journal of Computational Physics* 1967; **2**:12–26.
31. Codina R, Coppola-Owen H, Nithiarasu P, Liu C-B. Numerical comparison of CBS and SGS as stabilization techniques for the incompressible Navier–Stokes equations. *International Journal for Numerical Methods in Engineering* 2006; **66**:1672–1689.
32. Fernández MA, Gerbeau J-F, Grandmont C. A projection semi-implicit scheme for the coupling of an elastic structure with an incompressible fluid. *International Journal for Numerical Methods in Engineering* 2007; **69**:794–821.
33. Li J, Renardy Y. Numerical study of flows of two immiscible liquids at low Reynolds number. *SIAM Review* 2000; **42**:417–439.
34. Ni M-J, Abdou MA. A bridge between projection methods and SIMPLE type methods for incompressible Navier–Stokes equations. *International Journal for Numerical Methods in Engineering* 2007; **72**:1490–1512.
35. Harlow FH, Welch JE. Numerical calculation of time-dependent viscous incompressible flow of fluid with free surface. *Physics of Fluids* 1965; **8**:2182–2189.
36. Trottenberg U, Oosterlee C, Schüller A. *Multigrid*. Academic press: London, 2001.
37. Kim J. A numerical method for the Cahn–Hilliard equation with a variable mobility. *Communications in Nonlinear Science and Numerical Simulation* 2007; **12**:1560–1571.
38. Kim J, Bae H-O. An unconditionally stable adaptive mesh refinement for Cahn–Hilliard equation. *Journal of the Korean Physical Society* 2008; **53**:672–679.
39. Tryggvason G. Numerical simulations of the Rayleigh–Taylor instability. *Journal of Computational Physics* 1988; **75**:253–282.

DOI: 10.1002/nme